nature synthesis

Article

https://doi.org/10.1038/s44160-026-01179-1

Enhanced neutral seawater photoelectrolysis by fast hydrogen pumping at subnanometre triple interfaces

Received: 19 November 2025

Accepted: 14 September 2026

Published online: 30 October 2026

Check for updates

Bingxing Zhang[1,7] ✉, Kejian Li[1,7], Zhuoran Long[2,7], Shiyuan Zhou[3], Deming Xia[4] ✉, Chengjun Sun[5], Zhengwei Ye[1], Yuyang Pan[1], Jan Paul Menzel[2], Kai Sun[6], Joseph S. Francisco[4], Gui-Liang Xu[3], Victor S. Batista[2] ✉ & Zetian Mi[1] ✉

Hydrogen production from neutral water is promising for directly using abundant seawater, yet remains challenging because of sluggish reaction kinetics induced by limited hydrogen supply and transfer to active sites. Here we design a catalyst system consisting of atomically dispersed $Cr(OH)_x$ clusters on Pt-decorated GaN nanowires for photoelectrochemical splitting of neutral seawater. The triple-interface architecture ($Cr(OH)_x$–Pt//$Cr(OH)_x$–GaN//Pt–GaN) couples water activation, hydrogen transfer and Pt–H formation across adjacent interfaces, enabling a fast hydrogen pumping process. Through this process, the challenges associated with hydrogen supply and transfer are addressed, surpassing the kinetically limited hydrogen utilization on the conventional single-interface systems. A photocurrent density of around 100 mA cm^{-2} and more than 50 h of operational stability are achieved under neutral saline conditions with concentrated sunlight at 0 V versus the reversible hydrogen electrode. In a hydrazine-assisted seawater photoelectrolyser, the photocathode enables a bias-free photocurrent density of ~70 mA cm^{-2}. This work establishes multi-interface hydrogen management as a promising strategy towards practical hydrogen production.

The growing demand for sustainable and renewable energy sources has driven extensive research into efficient and environmentally friendly hydrogen production technologies[1]. Hydrogen is widely recognized as a promising clean energy carrier, offering high energy density and zero-emission combustion, making it a viable solution to address global energy and environmental challenges[2]. Among various approaches, photoelectrochemical (PEC) water splitting has emerged as one of the most promising strategies for sustainable hydrogen production[3–8]. This method harnesses solar energy in real time to store it as hydrogen energy while minimizing electrical power consumption and loss. However, practical implementation of PEC systems remains hindered by challenges such as limited photocurrent density and poor stability, particularly in neutral solutions or seawater environments[9–15].

High-concentration acidic and alkaline electrolytes are commonly used to achieve high hydrogen production rates in electrolysers, as they efficiently supply protons or facilitate water dissociation to provide

[1]Department of Electrical Engineering and Computer Science, University of Michigan, Ann Arbor, MI, USA. [2]Department of Chemistry, Quantum Institute and Energy Sciences Institute, Yale University, New Haven, CT, USA. [3]Chemical Sciences and Engineering Division, Argonne National Laboratory, Lemont, IL, USA. [4]Department of Earth and Environmental Science, University of Pennsylvania, Philadelphia, PA, USA. [5]Advanced Photon Source, Argonne National Laboratory, Lemont, IL, USA. [6]Michigan Center for Materials Characterization, University of Michigan, Ann Arbor, MI, USA. [7]These authors contributed equally: Bingxing Zhang, Kejian Li, Zhuoran Long. ✉e-mail: bingxinz@umich.edu; xiadm@sas.upenn.edu; victor.batista@yale.edu; ztmi@umich.edu

https://doi.org/10.1038/s44160-026-01179-1

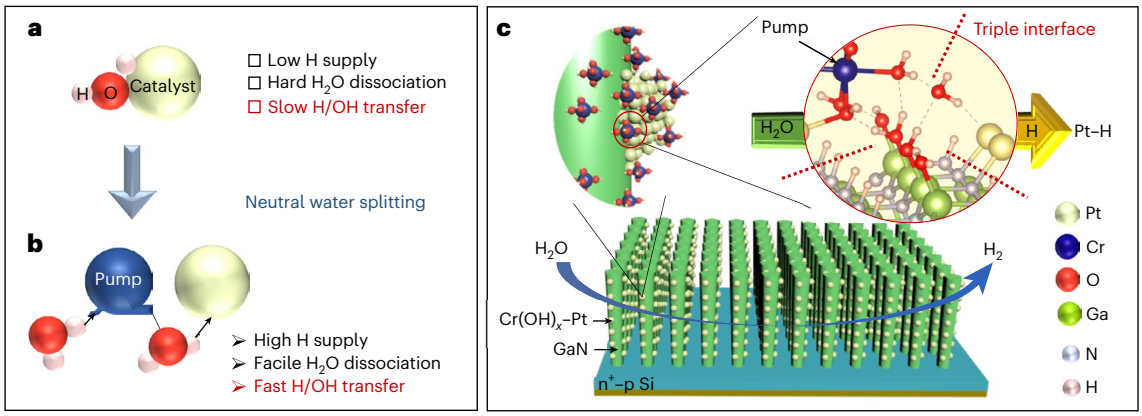


Fig. 1 | Scheme illustrations of the subnanometre interfacial hydrogen-pump-like mechanism for solving the challenges in neutral water splitting and the corresponding catalyst structure design. a, Challenges associated with neutral water splitting, including low hydrogen supply, inefficient water dissociation and restricted H/OH transfer processes. **b**, Proposed SIHP to address these limitations. The SIHP accelerates water dissociation and facilitates efficient hydrogen transfer to the catalyst. **c**, Schematic of atomically dispersed $Cr(OH)_x$ clusters on Pt-decorated GaN NWs supported by n^+–p Si photocathode, featuring a triple-interface configuration ($Cr(OH)_x$–Pt//$Cr(OH)_x$–GaN//Pt–GaN). The single-Cr-hydroxyl cluster acts as the fast hydrogen pump, enhancing water splitting to hydrogen under neutral conditions.

protons around the catalyst during the hydrogen evolution reaction (HER)[16,17]. However, using acidic or alkaline seawater leads to high chemical costs, as well as corrosion of catalysts, membranes and photoelectrodes, undermining stability, efficiency and scalability[18,19]. By contrast, neutral water splitting offers a more practical and cost-efficient solution by enabling the direct utilization of abundant water sources including seawater[20,21]. Despite this advantage, the slower kinetics of water splitting in neutral solutions, compared with acidic and alkaline conditions, has remained a major bottleneck in both electrocatalysis and photoelectrocatalysis[22,23]. Key challenges include insufficient hydrogen supply, sluggish water dissociation kinetics (Volmer step) and slow H/OH transfer kinetics intrinsic to neutral conditions[24–26] (Fig. 1a).

Efforts to address these limitations in neutral conditions have primarily focused on modifying the local reaction environment to mimic acidic or alkaline conditions through catalyst design[27–29]. However, these mechanisms rely on water adsorption and dissociation on specific sites, leaving possibly bound OH/H species that are unfavourable to transfer. The multistep process is kinetically limited and thus impedes efficient proton delivery to active sites[16,27–29]. These issues are further exacerbated in seawater owing to its chemical complexity, leading to a substantial drop in performance compared to freshwater electrolysis[27–32]. Moreover, under PEC conditions, additional challenges such as photocorrosion, photodegradation and cocatalyst-induced suppression of photoabsorption must be overcome[7,33–36].

To address these challenges, here we propose a subnanometre interfacial hydrogen-pump (SIHP)-like mechanism for solar-assisted water splitting in neutral seawater (Fig. 1b). This SIHP efficiently dissociates interfacial water to supply hydrogen on the catalyst while extracting hydrogen from free water to replenish the consumed interfacial water. The transfer of H and OH species is thus substantially accelerated via the SIHP pathway, establishing a more efficient and integrated route for rapid hydrogen reaction kinetics compared with conventional strategies.

We adopt this concept using atomically dispersed chromium hydroxide ($Cr(OH)_x$) clusters anchored on Pt/GaN NW/Si as photocathodes, enabling fast hydrogen pumping (Fig. 1c). The single-metal $Cr(OH)_x$ cluster enables a subnanometre triple-interface configuration ($Cr(OH)_x$–Pt//$Cr(OH)_x$–GaN//Pt–GaN), which powers water dissociation and accelerates H/OH transfer via the SIHP, enabling the fast formation of Pt–H sites and keeping the photoabsorption properties of the photocathode. This design delivers a high photocurrent density (~100 mA cm^{-2}) and stability (>50 h) in a flow-cell under neutral saline conditions and concentrated sunlight at 0 V versus the reversible hydrogen electrode (RHE). Furthermore, a bias-free hydrazine-assisted seawater photoelectrolyser was demonstrated, achieving ~70 mA cm^{-2} and surpassing previously reported solar-assisted systems operating in more favourable acidic or alkaline freshwater electrolytes. This approach not only establishes a practical and efficient strategy for sustainable hydrogen production from neutral seawater, but also offers a promising interfacial hydrogen-pump-like mechanism for hydrogen catalysis and clean energy technologies.

Results and discussion

Material design and structure

GaN nanowires (NWs) arrays, approximately 300 nm in length and ~50 nm in diameter, were grown on an n^+–p Si wafer using molecular beam epitaxy (Supplementary Fig. 1), which has strong capability for photogenerated charge separation and efficient electron transfer to the metal catalyst for hydrogen evolution (Supplementary Fig. 2). The $Cr(OH)_x$–Pt/GaN/Si photocathode was then obtained via simultaneous photodeposition of chloroplatinic acid and chromic nitrate on the GaN surface by well-controlled deposition parameters and precursor selection (Methods and Supplementary Fig. 3). During this process, metallic platinum nanoparticles (Pt NPs) are deposited concurrently with the formation of $Cr(OH)_x$ clusters on the GaN NW surface through competitive consumption of photogenerated electrons. The subnanometre triple interfaces were thus created by bridging the Pt/GaN interface with a single-metal $Cr(OH)_x$ cluster. Scanning electron microscopy (SEM) images of the $Cr(OH)_x$–Pt/GaN/Si photocathode revealed well-aligned NWs with abundant deposited particles (Supplementary Fig. 4), consistent with scanning transmission electron microscopy high-angle annular dark-field (STEM-HAADF) imaging observations (Fig. 2a). Energy-dispersive X-ray spectroscopy (EDS) mapping confirmed the homogeneous dispersion of Cr and Pt species across the entire GaN NW surface (Fig. 2b).

Enlarged STEM-HAADF images for $Cr(OH)_x$–Pt/GaN revealed Pt NPs (~1.5 nm in size) anchored on the GaN NW surface, characterized by the Pt (111) facet with a lattice spacing of 0.23 nm (Fig. 2c and Supplementary Fig. 5). No amorphous layers or aggregated Cr oxides were observed on the Pt NPs or the GaN NW surface, suggesting the presence of atomically dispersed Cr-oxide clusters. The Pt NPs in the $Cr(OH)_x$–Pt/GaN/Si system feature low-coordinated surfaces due to their ultrasmall size and stabilization by $Cr(OH)_x$ clusters (Supplementary Figs. 6 and 7), providing highly active sites for HER[17]. In the absence of Pt, the synthesized $Cr(OH)_x$–GaN/Si exhibits a continuous subnanometre Cr–O layer on the GaN surface

https://doi.org/10.1038/s44160-026-01179-1

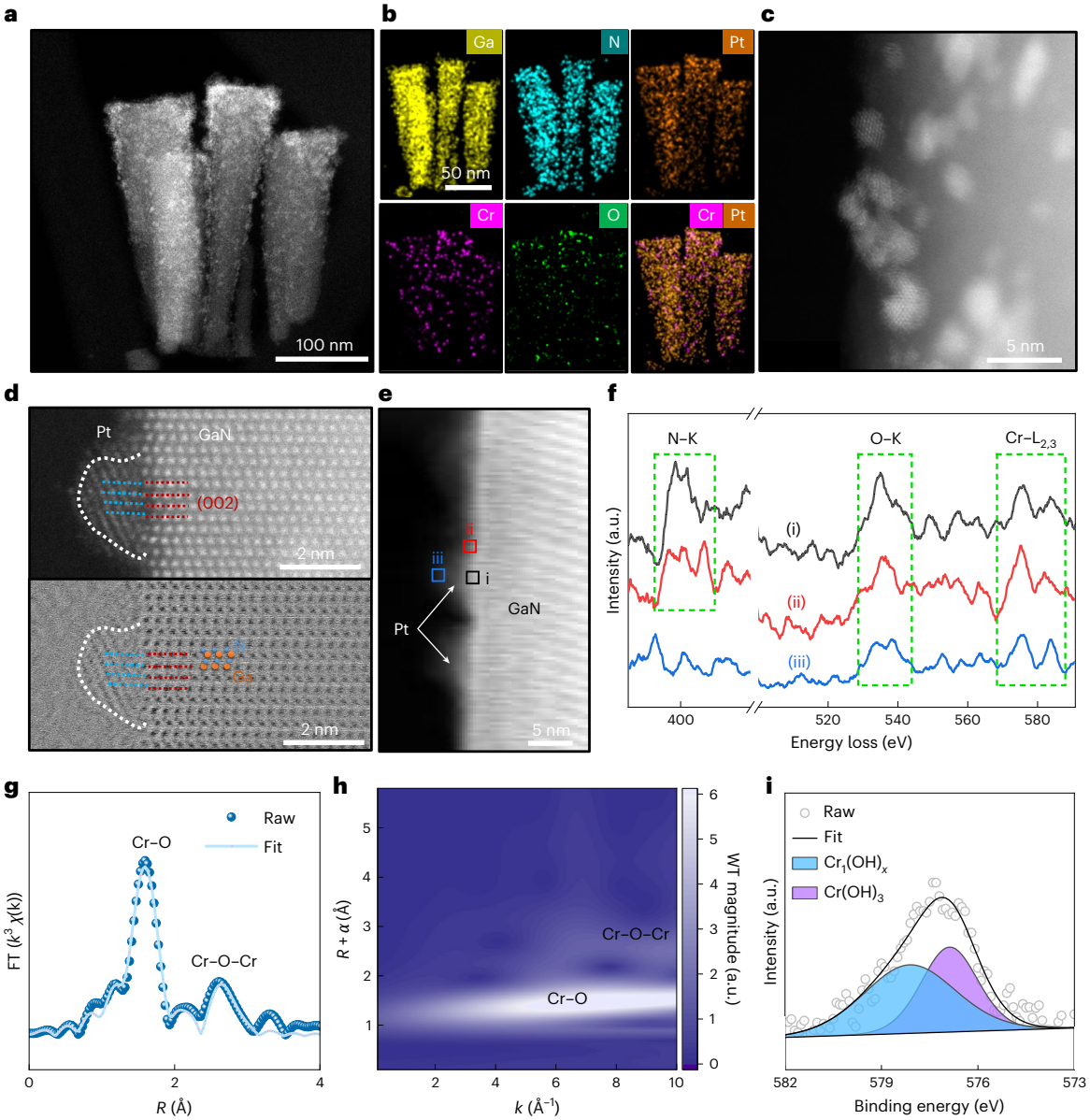


Fig. 2 | Structural characterizations of $Cr(OH)_x$–Pt/GaN. a,**b**, STEM-HAADF image (**a**) and corresponding EDS elemental map (**b**) of the entire NWs. **c**, Enlarged STEM-HAADF image. **d**, STEM-HAADF image (top) and STEM differential phase contrast (bottom) showing the atomic structure. **e**,**f**, STEM-HAADF image with the corresponding EELS spectra collecting areas outlined (**e**) and the EELS spectra (**f**) extracted from the outlined regions in **e**. **g**, Cr K-edge EXAFS fitting curves. **h**, WT for the k^3-weighted EXAFS. **i**, XPS spectra of the Cr 2*p* region.

(Supplementary Fig. 8), indicating that the presence of Pt NPs induces the formation of atomically dispersed $Cr(OH)_x$ species on $Cr(OH)_x$–Pt/GaN/Si. The Pt NP size was further tuned by varying the amount of Pt precursor, revealing that increasing the Pt precursor amount leads to larger Pt particles and more dispersed $Cr(OH)_x$ species (Supplementary Figs. 9–11), supporting the proposed optimization strategy for synthesizing $Cr(OH)_x$–Pt/GaN/Si.

The $Cr(OH)_x$–Pt/GaN structure exhibits some epitaxial alignment between the GaN (002) plane and the Pt (111) facet (Fig. 2d). The epitaxial structure is expected to enhance operational stability by maintaining a stable and well-defined interface that interacts with the $Cr(OH)_x$ clusters, which serve as active structures for the accelerated HER. High-resolution EDS mapping further confirmed the uniform distribution of atomically dispersed Cr species across the Pt NPs without extending beyond their boundaries (Supplementary Fig. 12a). Layer-by-layer EDS profile spectra from the outer Pt NP surface to the interface reinforced the spatial correlation between Pt and Cr species (Supplementary Fig. 12b). These results collectively highlight the successful integration of atomically dispersed Cr species onto Pt NPs and the GaN surface, forming an effective triple-interface structure ($Cr(OH)_x$–Pt//$Cr(OH)_x$–GaN//Pt–GaN). To further verify this, high-resolution and chemically sensitive electron energy loss spectroscopy (EELS) spectra analysis were performed along the $Cr(OH)_x$–Pt/GaN interface (Fig. 2e,f). It is obvious that the $Cr(OH)_x$ species (based on Cr and O EELS spectra) clearly interacted with Pt (based on HAADF-STEM imaging) and GaN (based on N EELS spectra) at the triple-interface region, further supporting the spatial distribution of the proposed triple-interface structure.

To further confirm the presence of atomically dispersed $Cr(OH)_x$ species in the system, we performed the X-ray absorption spectroscopy (XAS) measurements for the $Cr(OH)_x$–Pt/GaN sample (Fig. 2g,h, Supplementary Figs. 13 and 14 and Supplementary Table 1). The Fourier transform extended X-ray absorption fine structure (EXAFS) spectra (Fig. 2g) and wavelet transform (WT) for EXAFS (Fig. 2h) confirm that

https://doi.org/10.1038/s44160-026-01179-1

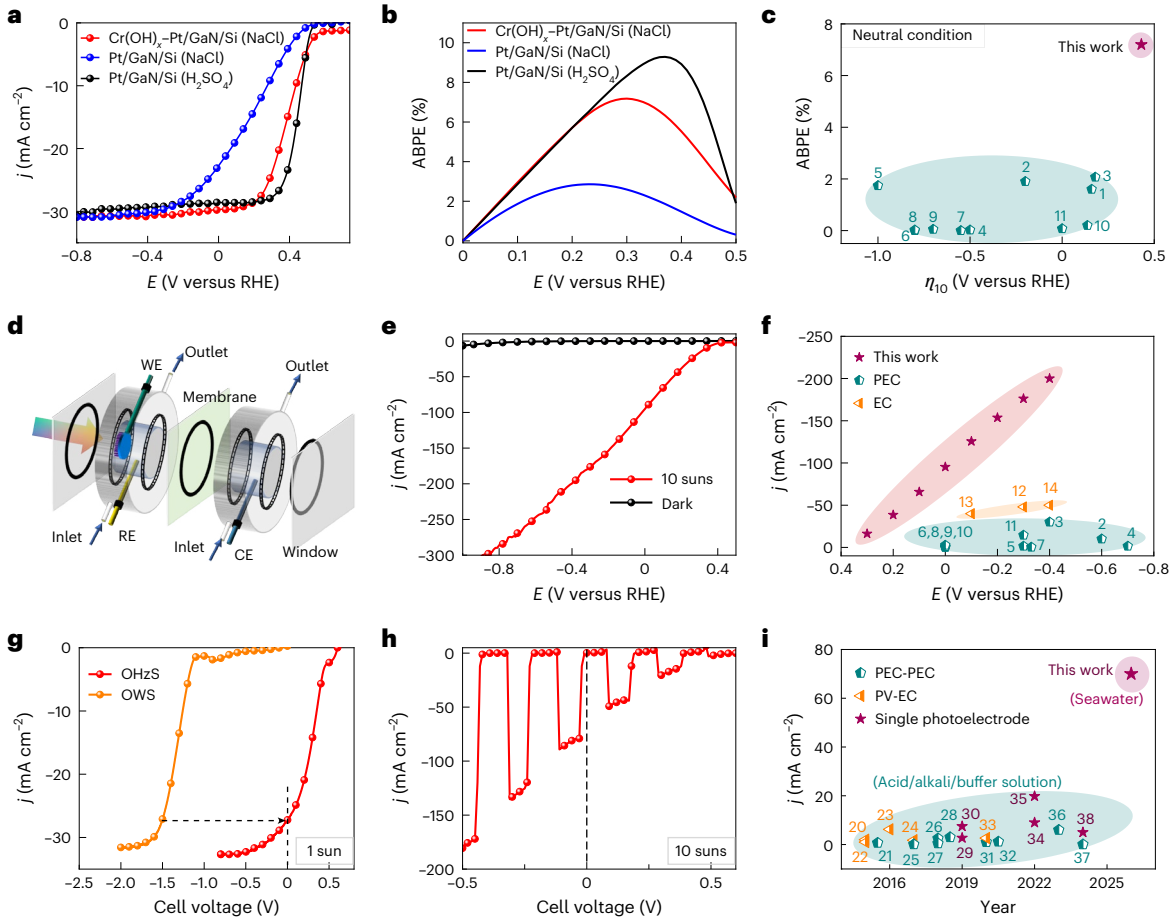


Fig. 3 | PEC HER performances. a–c, Non-concentrating system: LSV curves obtained with a three-electrode configuration in 0.5 M NaCl (neutral) or 0.5 M H_2SO_4 (acidic) solution under AM1.5G 1-sun illumination (**a**); ABPE curves as a function of applied potentials (**b**); comparison of the ABPE and the applied potential at −10 mA cm^{-2} (η_{10}) of $Cr(OH)_x$–Pt/GaN/Si photocathodes with those in the literature in neutral condition (**c**). **d–f**, Concentrating system: schematic illustration of the PEC flow cell system designed for water splitting under concentrated sunlight (**d**); LSV curves of the $Cr(OH)_x$–Pt/GaN/Si photocathode measured in 0.5 M NaCl solution under dark and 10-sun illumination (**e**); comparison of HER photocurrents achieved in neutral saline water of this work with the maximum photocurrents reported in the literature and the low-bias currents of state-of-the-art electrochemical (EC) catalysts (**f**). **g–i**, Bias-free system: LSV curves of the cell systems for overall water splitting (OWS) with anodic oxygen evolution and overall hydrazine splitting (OHzS) with anodic hydrazine oxidation (**g**); LSV curves of the $Cr(OH)_x$–Pt/GaN/Si photocathode during N_2H_4-assisted seawater splitting under chopped illumination (**h**); comparison of photocurrent achieved in this study against the highest reported photocurrents for bias-free neutral water splitting systems in the literature (**i**). PEC–PEC, dual-photoelectrode PEC configurations; PV-EC, photovoltaic-assisted EC systems. The numbers 1–14 and 20–38 in **c**, **f** and **i** correspond to the references listed in Supplementary Tables 2, 3 and 5, respectively. CE, counter electrode; RE, reference electrode; WE, working electrode.

$Cr(OH)_x$–Pt/GaN exhibits atomically dispersed Cr species, primarily featuring a Cr_1–O_6 local coordination environment, with a minor contribution from Cr–O–Cr interactions in the second scattering shell.

X-ray photoelectron spectroscopy (XPS) provides further insights into the surface chemical states of $Cr(OH)_x$–Pt/GaN/Si. As shown in Fig. 2i, the Cr $2p_{3/2}$ XPS spectra of the $Cr(OH)_x$–Pt/GaN/Si sample revealed two chemical states: Cr(III) trivalent hydroxide (576.7 eV) state and Cr(III) coordinated with additional hydroxyl ligands in single-Cr-hydroxyl cluster ($Cr_1(OH)_x$) at 578.0 eV (ref. 37). In comparison with the Cr $2p_{3/2}$ spectrum of the $Cr(OH)_x$/GaN/Si sample (Supplementary Fig. 15a), these results indicate that Pt–$Cr(OH)_x$ interactions promote the formation of more atomically dispersed $Cr_1(OH)_x$ species, consistent with above STEM characterization results. The Pt 4*f* XPS spectra displayed two doublets of ($4f_{5/2}$ and $4f_{7/2}$), corresponding primarily to metallic Pt bonds (71.6 and 74.9 eV) and a minor fraction of Pt^{2+} species (72.7 and 76.3 eV) (Supplementary Fig. 15b). A higher Pt^{2+} signal is observed in the $Cr(OH)_x$–Pt/GaN/Si sample, suggesting the introduction of $Cr(OH)_x$–Pt interactions. The Ga 3*d* spectra show increased Ga–O signals in both $Cr(OH)_x$/GaN/Si and $Cr(OH)_x$–Pt/GaN/Si samples, suggesting formed Ga–O interactions between $Cr(OH)_x$ and GaN (Supplementary Fig. 15c). The positively shifted N 1*s* spectra in both $Cr(OH)_x$–Pt/GaN/Si and Pt/GaN/Si samples, compared with the other two samples, suggest the formation of Pt–N interactions at the Pt–GaN interface (Supplementary Fig. 15d). These results collectively support that the atomically dispersed $Cr(OH)_x$ clusters interact with GaN and Pt to form a triple-interface catalytic architecture that potentially offers a distinctive pathway to enhance HER activity and stability.

PEC HER performance in neutral saline water

The photocathode for PEC HER was assessed using three-electrode configuration under Air Mass 1.5 Global (AM 1.5 G) illumination (1 sun) in various electrolytes. The Pt/GaN/Si photocathode was initially evaluated in 0.5 M NaCl (pH 7.4) and 0.5 M H_2SO_4 (pH 0) solutions to study the impact of pH on HER performance (Fig. 3a). Pt/GaN/Si exhibited lower HER activity in neutral NaCl solution compared with the acidic solution due to limited proton availability near the electrode surface. The applied bias photon-to-current efficiency (ABPE, 2.9%) and half-wave potential ($E_{1/2}$, 0.17 V) of Pt/GaN/Si in neutral conditions are much lower than those (9.3% and 0.44 V) in acidic condition (Supplementary Fig. 16). Furthermore, the Pt–GaN interface was crucial to achieve efficient

neutral water splitting since the Pt/Si photocathode shows negligible HER activity at low overpotentials (Supplementary Fig. 17).

The $Cr(OH)_x$–Pt/GaN/Si photocathode was designed to overcome challenges related to proton availability and H/OH transfer in neutral water splitting. This design substantially improved HER activity in the neutral NaCl solution, achieving a high ABPE of 7.2% and $E_{1/2}$ of 0.38 V versus RHE, approaching the performance observed in acidic conditions (Fig. 3a,b and Supplementary Fig. 16). The $Cr(OH)_x$–Pt/GaN/Si photocathode shows a Tafel slope of 139.5 mV dec^{-1}, indicating a Volmer-limited HER process with markedly improved kinetics compared with Pt/GaN/Si (Supplementary Fig. 18). The system achieved among the highest performances reported for PEC systems operating under neutral electrolyte conditions (Fig. 3c and Supplementary Table 2). However, excessive $Cr(OH)_x$ deposition resulted in reduced activity due to a loss in photoabsorption, as the amorphous layer hindered light penetration (Supplementary Fig. 19). These results demonstrate that the strategic incorporation of atomically dispersed $Cr(OH)_x$ species can efficiently address the activity problems in neutral PEC systems, without compromising photocurrent generation. Further PEC measurements were conducted to determine the optimal loading conditions by controlling the Pt precursor addition to yield the optimal Pt loading, which coincides with the optimal $Cr(OH)_x$ deposition on the photocathode (Supplementary Figs. 9–11 and 20).

PEC measurements of the $Cr(OH)_x$/GaN/Si photocathode indicate that the $Cr(OH)_x$–GaN interface markedly enhances the HER activity of GaN (Supplementary Fig. 21), while the Pt–$Cr(OH)_x$ interface shows only a marginal effect on Pt activity (Supplementary Fig. 22). These results highlight the crucial role of the $Cr(OH)_x$–GaN interface in facilitating hydrogen transfer within the triple-interface structure of $Cr(OH)_x$–Pt/GaN, which is further supported by control experiments using an AlO_x passivation layer on GaN surface (Supplementary Fig. 23 and Note 1).

To explore the practical application of this system, a PEC flow cell was designed to operate water splitting under concentrated solar illumination (Fig. 3d and Supplementary Fig. 24). Concentrated sunlight increased photocurrent generation, reduced electrode area, improved space utilization and lowered system costs, while the flow cell enhanced mass transport and gas removal, enabling high H_2 production rates. The PEC HER process was conducted with a 0.5-M NaCl solution flow. As light intensity increased from 0.6 to 3 suns, the maximum current rose from 21 to ~100 mA cm^{-2} (Supplementary Fig. 25). Under 10-sun illumination, a high photocurrent density of ~300 mA cm^{-2} could be achieved (Fig. 3e), much higher than previously reported water splitting systems (Fig. 3f and Supplementary Table 3). These photocurrent densities under low-bias condition are even comparable to those in electrolysers, despite the relatively small specific surface area of the wafer photocathode (Supplementary Figs. 26–28, Supplementary Table 3 and Supplementary Note 2). In addition, the applied bias required to achieve high current densities (~100 mA cm^{-2} at 0 V versus RHE) was substantially lower than in typical systems.

Long-term stability measurements conducted under 10 suns at 0 V vs RHE suggested relatively stable photocurrent densities near 100 mA cm^{-2} for over 50 h (Supplementary Fig. 29). Post-reaction characterization via SEM, EDS mapping, high-resolution STEM, EELS mapping images and XPS spectra indicated the structural robustness in chemical state or morphologies of the photocathode (Supplementary Figs. 30–32), while the possible performance degradation may be attributed to the loss of Pt species after the long-time operation.

The designed photocathode for PEC hydrogen evolution demonstrates consistent performance under both actual sunlight and standard AM 1.5 G illumination (Supplementary Fig. 33), thereby confirming the uniformity of the performance comparison for practical applications. In addition, the enlarged photoelectrode exhibited uniform catalytic structures (Supplementary Fig. 34) and high photocurrent densities under 50-fold concentrated sunlight (Supplementary Fig. 35), demonstrating the promising scalability solar hydrogen applicability of the proposed system.

Photoelectrolyser performance for neutral seawater splitting

The PEC performance of neutral seawater splitting was evaluated using a $Cr(OH)_x$–Pt/GaN/Si photocathode. The photocathode demonstrated an ABPE of 7.0%, comparable to its performance in 0.5 M NaCl solution (Supplementary Fig. 36). For practical photoelectrolysis applications, overall water splitting performances were measured in seawater solution using a two-electrode configuration with a RuO_x anode grown on Ti mesh under concentrated 10-sun illumination (Supplementary Fig. 37a), achieving a much lower cell voltage to reach 10 mA cm^{-2} (Supplementary Table 4). The high Faradaic efficiencies of H_2 and O_2 under various light intensities and applied potentials (Supplementary Fig. 37b,c) further indicate this efficient overall seawater splitting system.

We further integrated the $Cr(OH)_x$–Pt/GaN/Si photocathode for HER with an anode N_2H_4 oxidation to construct the bias-free seawater-splitting device based on a single photoelectrode (Supplementary Fig. 38). N_2H_4 oxidation reaction features a much lower oxidation potential and faster kinetics than oxygen evolution reaction, enabling high-rate, bias-free PEC operation in seawater. This strategy not only results in energy savings while utilizing N_2H_4, often considered waste or a contaminant, as a reactant[38,39], but also eliminates the need for gas separation between O_2 and H_2, thereby reducing safety risks and simplifying system design (Supplementary Note 3). Figure 3g shows linear sweep voltammetry (LSV) scans of the $Cr(OH)_x$–Pt/GaN/Si photocathode coupled with oxygen evolution reaction and N_2H_4 oxidation in seawater, demonstrating the effectiveness of the bias-free hydrazine oxidation-assisted H_2 production system.

The introduction of $Cr(OH)_x$ clusters enhanced reaction kinetics, enabling the $Cr(OH)_x$–Pt/GaN/Si photocathode system to achieve a higher current density of 27 mA cm^{-2} under 1-sun illumination (Supplementary Fig. 39). Under concentrated 10-sun illumination, the photocurrent density further promoted to ~70 mA cm^{-2} in a bias-free neutral configuration (Fig. 3h and Supplementary Note 4). Under varying potentials and light intensities, bias-free PEC seawater splitting shows high Faradaic efficiencies for both H_2 and N_2 in hydrazine-assisted water splitting (Supplementary Fig. 40), indicating highly selective charge utilizations. The system also exhibited a good stability, achieving a high photocurrent density for >15 h of bias-free operation (Supplementary Fig. 41).

The bias-free photocurrent density of ~70 mA cm^{-2} represents among the best of solar hydrogen production systems, including single-photoelectrode and dual-photoelectrode PEC configurations, as well as photovoltaic-assisted electrochemical water splitting devices (Fig. 3i and Supplementary Table 5). Notably, this system operates in neutral seawater, offering a more practical and scalable solution compared with previous systems that require buffered solutions or highly alkaline/acidic freshwater electrolytes.

Mechanism studies

Comprehensive experiments and computational studies were conducted to elucidate the mechanism underlying the high HER activity of the $Cr(OH)_x$–Pt/GaN/Si photocathode. After selectively removing $Cr(OH)_x$ from $Cr(OH)_x$–Pt/GaN by strong-acid etching, the HER activity dropped to a level close to that of Pt/GaN (Supplementary Figs. 42 and 43 and Supplementary Note 5), excluding contributions from Pt size/coordination and Pt–support electronic effects. In addition, hydrogen desorption measurements show that $Cr(OH)_x$ incorporation does not measurably alter the hydrogen behaviour on Pt (Supplementary Fig. 44), thereby ruling out electronic structure change of Pt (Supplementary Note 5). The H/D kinetic isotope effect values for $Cr(OH)_x$–Pt/GaN/Si decrease from 1.45 to 1.25 at lower potentials, compared with

https://doi.org/10.1038/s44160-026-01179-1

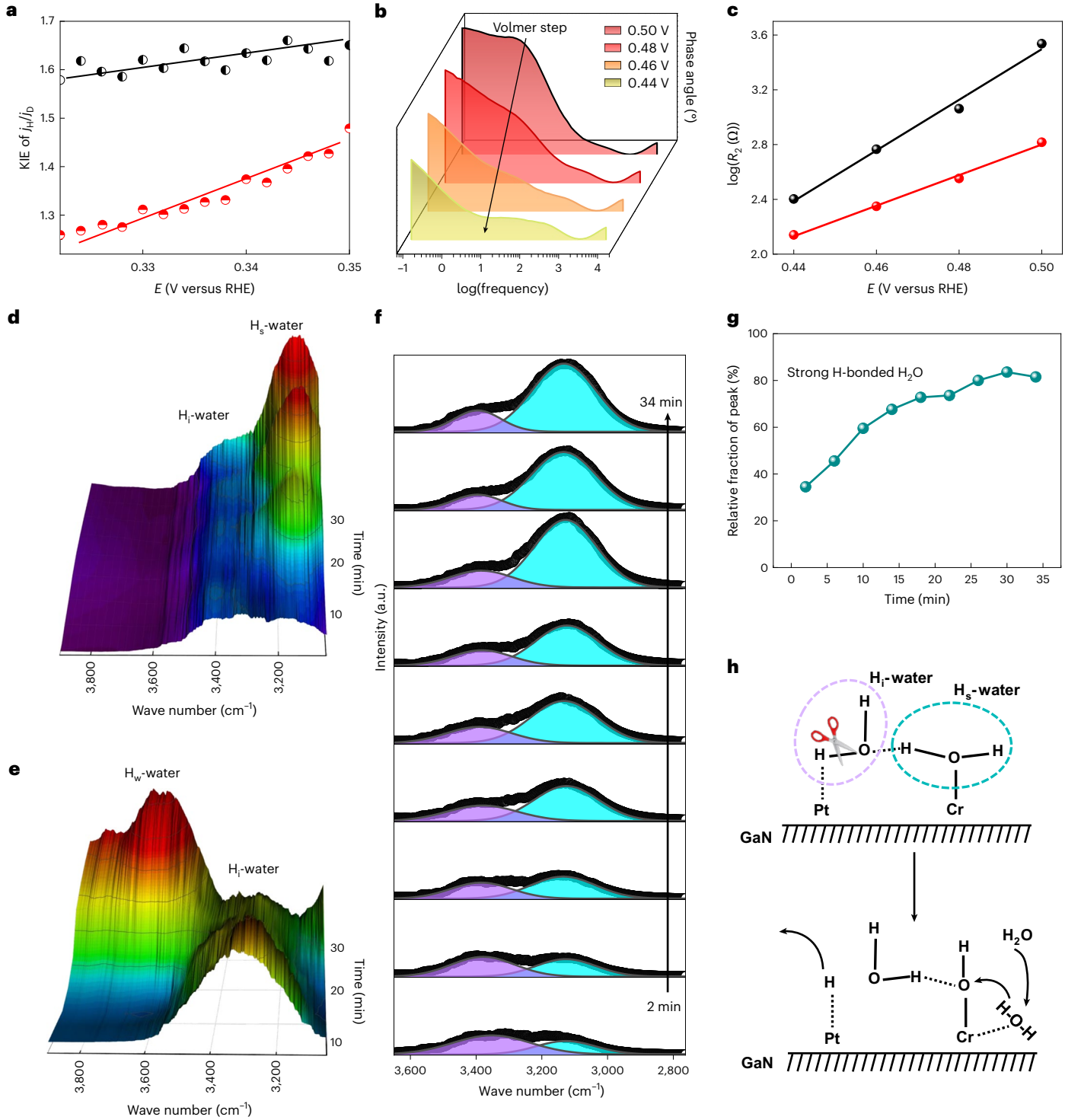


Fig. 4 | Mechanism characterization. a, Kinetic isotope effect (KIE) values as a function of potential for $Cr(OH)_x$–Pt/GaN/Si (red) and Pt/GaN/Si (black) in D_2O and H_2O solutions with 0.5 M NaCl. **b**, Bode phase plots from operando EIS measurements on $Cr(OH)_x$–Pt/GaN/Si during PEC HER. **c**, EIS-derived Tafel plots for hydrogen adsorption resistance (R_2) of $Cr(OH)_x$–Pt/GaN/Si (red) and Pt/GaN/Si (black). **d**,**e**, Three-dimensional surface plots of in situ ATR-FTIR spectra for $Cr(OH)_x$–Pt/GaN/Si (**d**) and Pt/GaN/Si (**e**) at 0 V versus RHE. H_s, H_i and H_w represent the strongly, intermediately and weakly hydrogen-bonded water, respectively. **f**, Deconvolution of OH stretching peaks from in situ ATR-FTIR spectra of $Cr(OH)_x$–Pt/GaN/Si. **g**, Relative fraction of strongly bonded water as a function of time. **h**, Schematic of H_s-water promotion in water dissociation and H/OH transport.

Pt/GaN/Si, which exhibits a higher H/D isotope effect of 1.6–1.7 (Fig. 4a). This indicates that $Cr(OH)_x$–Pt/GaN/Si facilitates a faster water dissociation and hydrogen transfer by accelerating the Volmer step[40] (Supplementary Note 5).

To further investigate hydrogen transfer kinetics during the reaction, operando electrochemical impedance spectroscopy (EIS) was used. The Bode phase plots for $Cr(OH)_x$–Pt/GaN/Si reveal that the phase angle in the low-frequency region, associated with the Volmer step, decreases more rapidly than that of Pt/GaN/Si (ref. 41) (Fig. 4b, Supplementary Fig. 45). This corroborates the accelerated Volmer step facilitated by $Cr(OH)_x$–Pt/GaN/Si. Hydrogen transfer resistance can be analysed by the second parallel component (R_2) from

quantitatively fitting the Nyquist plots[42] (Supplementary Figs. 46 and 47). EIS-derived Tafel plots of logR_2 versus applied potential for Cr(OH)$_x$–Pt/GaN/Si demonstrate substantially reduced hydrogen transfer resistance compared to Pt/GaN/Si (Fig. 4c), indicating enhanced hydrogen transfer kinetics. Considering the Pt sites in the two systems have an identical hydrogen behaviour (Supplementary Fig. 44), the above results imply that Cr(OH)$_x$ functions analogously to a hydrogen pump, facilitating a rapid hydrogen transfer to Pt sites for HER (Supplementary Note 5).

In situ attenuated total reflection Fourier transform infrared (ATR-FTIR) spectroscopy under photoelectrochemistry condition was used to examine the influence of interfacial water structures during the PEC HER process[43–45] (Fig. 4d,e and Supplementary Figs. 48 and 49). Weakly bonded water (H_w-water) typically exhibits ν(OH) bands at ~3,600 cm^{-1}. In addition, hydrogen bonding among water molecules induces a redshift and broadening of these bands, with a more pronounced effect for hydrogen donors than for hydrogen acceptors[43,44].

No obvious H_w-water peaks were observed for the Cr(OH)$_x$–Pt/GaN/Si sample, indicating the formation of a robust hydrogen-bond network. A broad band at approximately 3,120 cm^{-1} was detected, associated with strongly hydrogen-bonded water molecules acting as hydrogen donors[46] (H_s-water, highlighted by the blue circle in Fig. 4h). In the Cr(OH)$_x$ species, the readily coordinated Cr sites promote the formation of this conformation due to their positive charges, which interact with the lone pairs of oxygen atoms in water through Lewis acid–base interactions. In addition, the band around ~3,340 cm^{-1} can be assigned to intermediate hydrogen-bonded water molecules[43,44] (H_i-water, shown by the purple circle in Fig. 4h), functioning as hydrogen acceptors.

The ν(OH) band of H_s-water was progressively dominant over time, accompanied by a sustained ν(OH) band for H_i-water (Fig. 4f,g). This evolution probably establishes a hydrogen-transfer gradient from H_s-water donor to H_i-water acceptor, thereby sustaining efficient interfacial hydrogen transfer (Fig. 4h and Supplementary Note 5). In this transfer process, the H from H_s-water interacts with the O in H_i-water, promoting H_i-water dissociation. The resulting OH binds with H from H_s-water to form a new H_i-water, maintaining a stable H_i-water structure. Then, the Cr site in Cr(OH)$_x$ attracts additional free water to form adjacent H_s-water, supplying H to regenerate the original H_s-water. Finally, the whole process is maintained through the continuous interaction of free water with H_2O ligands on Cr sites.

By contrast, this unique behaviour of ν(OH) bands is altered on the Pt/GaN/Si surface in the absence of Cr(OH)$_x$ species (Fig. 4e). The H_s-water band is not obvious, and the H_i-water band reduces gradually, accompanied by increased intensity and ratio of the H_w-water band (Fig. 4e). This indicates that the intermediately bonded interfacial water is progressively disrupted and similarly converted into free water owing to the absence of an interfacial hydrogen pump.

To further support the proposed mechanism, density functional theory (DFT) calculations and ab initio molecular dynamics (AIMD) simulations were performed to simulate the Pt/GaN interface with and without isolated $Cr_1(OH)_x$ clusters. To extract the dominant interfacial region and simplify the experimental system while maintaining computational efficiency, the Pt_3 cluster on GaN was selected to represent the Pt–GaN edge (Fig. 5a, Supplementary Fig. 50 and Supplementary Notes 6 and 7). The density of states analysis of Pt/GaN shows strong orbital coupling between Pt and GaN (Supplementary Fig. 51). The Cr(OH)$_6$ cluster on the Pt/GaN interface was selected for the simulation based on the EXAFS results (Fig. 2g,h and Supplementary Table 1). Further calculations of the pK_a values for Cr(OH)$_6$, Mo(OH)$_6$ and W(OH)$_6$ reveal a decreasing trend, which closely correlates with their PEC HER performances (Supplementary Figs. 52–54). This consistency highlights the unique role of Cr(OH)$_6$ in promoting water dissociation and facilitating H/OH transport partially due to its lowest pK_a value.

Simulations were conducted to evaluate the rate-determining Volmer step ($H_2O + e^- \rightarrow H_{ad} + OH^-$)[29,47] for HER under alkali and neutral conditions in the two systems. The results for Cr(OH)$_x$–Pt/GaN align closely with the in situ ATR-FTIR results. At the Cr(OH)$_x$–GaN interface, the interfacial H_i-water molecule establishes a hydrogen-bond network, facilitated by H donation from H_s-water to the O in H_i-water (Fig. 5b, red line). During the Volmer step, a Pt–H bond is formed while the generated OH obtains the H from H_s-water to form a new H_i-water molecule. The H transfer from adjacent H_s-water on Cr sites sustains H_s-water regeneration. This rate-determining step is highly exothermic, with a reaction energy change (ΔE) of −0.39 eV, further indicating the efficiency of the SIHP pathway at the Cr(OH)$_x$–Pt/GaN interface. Moreover, this SIHP mechanism accelerates OH transfer probably by confining the dissociated OH group within the interfacial water layer, avoiding strong binding to Pt sites and reducing desorption-related energy consumption. The migration of OH groups away from Pt sites preserves Pt–H sites, enhancing HER activity. Finally, the introduction of Cr(OH)$_x$ efficiently addresses the above kinetic problem without impairing photoabsorption on GaN/Si, thereby maintaining high photocurrent density. By contrast, the water dissociation on Pt sites during the Volmer step on Pt/GaN is endothermic, with a reaction energy change (ΔE) of 0.25 eV (Fig. 5b, blue). This reaction energy change leads to OH accumulation on Pt sites, hindering OH/H transfer and slowing the reaction process.

To further uncover the proposed SIHP mechanism, we performed AIMD simulations on the Cr(OH)$_x$–Pt/GaN interface with several H_2O molecules. The DFT-based vibrational analysis further predicts H_s-water and H_i-water bands that agree well with the experimental ATR-FTIR peaks (Fig. 4f, Supplementary Fig. 55 and Supplementary Note 5), indicating a relatively reasonable interfacial model. Specifically, we simulated the evolution of the Pt–H distance between the H_i-water and Pt, as well as the O–H distance associated with H transfer from H_s-water to H_i-water (Fig. 5c). The results reveal that, after the H transfer from H_s-water to H_i-water was completed at approximately 24.5 ps, the H_i-water H atom, which was initially pointing towards Pt, bonded with Pt to form Pt–H at around 25.8 ps (Fig. 5d). This suggests that the H-transfer process plays a crucial role in water dissociation, thereby replenishing the interfacial H_i-water for subsequent reactions.

To further quantify this process, we tracked the energy barrier for the overall evolution from the initial to the final state. The barrier remained consistently low, with a maximum value of only 0.19 eV on the Cr(OH)$_x$–Pt/GaN model (Fig. 5e), which is substantially lower than the transition barrier of 0.92 eV for the Volmer step on the Pt/GaN model (Supplementary Fig. 56). Molecular dynamics simulations of the Cr(OH)$_x$–GaN interface reveal that this boundary facilitates efficient hydrogen transfer from interfacial water molecules to the GaN surface (Supplementary Fig. 57), in agreement with experimental observations showing that such an interface facilitates hydrogen transfer and thereby enhances the HER (Supplementary Fig. 21). Representative evolved structures during the simulation are presented in Fig. 5f, illustrating that Cr(OH)$_x$ at the triple-interface region acts as a 'reservoir' to provide the H-transfer-water for dissociating interfacial water on Pt, while the other H_s-water molecules on Cr(OH)$_x$, extracted from bulk water, continuously replenishes the H-transfer process.

These combined experiment and simulation findings suggest that SIHP mechanism could reasonably serve as a promising mechanism interpretation for revealing the interfacial-water-regulated hydrogen electrocatalysis. Although the precise role of interfacial water in previous works has still been debated in the context of hydrogen-bond networks and hydroxyl-transfer mechanisms[46,48], the proposed SIHP model offers a complementary viewpoint by integrating these processes at the subnanometre triple interface. Nevertheless, future further advances in direct visualization techniques and multiscale simulation methods will be valuable for refining and validating this concept in greater detail.

https://doi.org/10.1038/s44160-026-01179-1

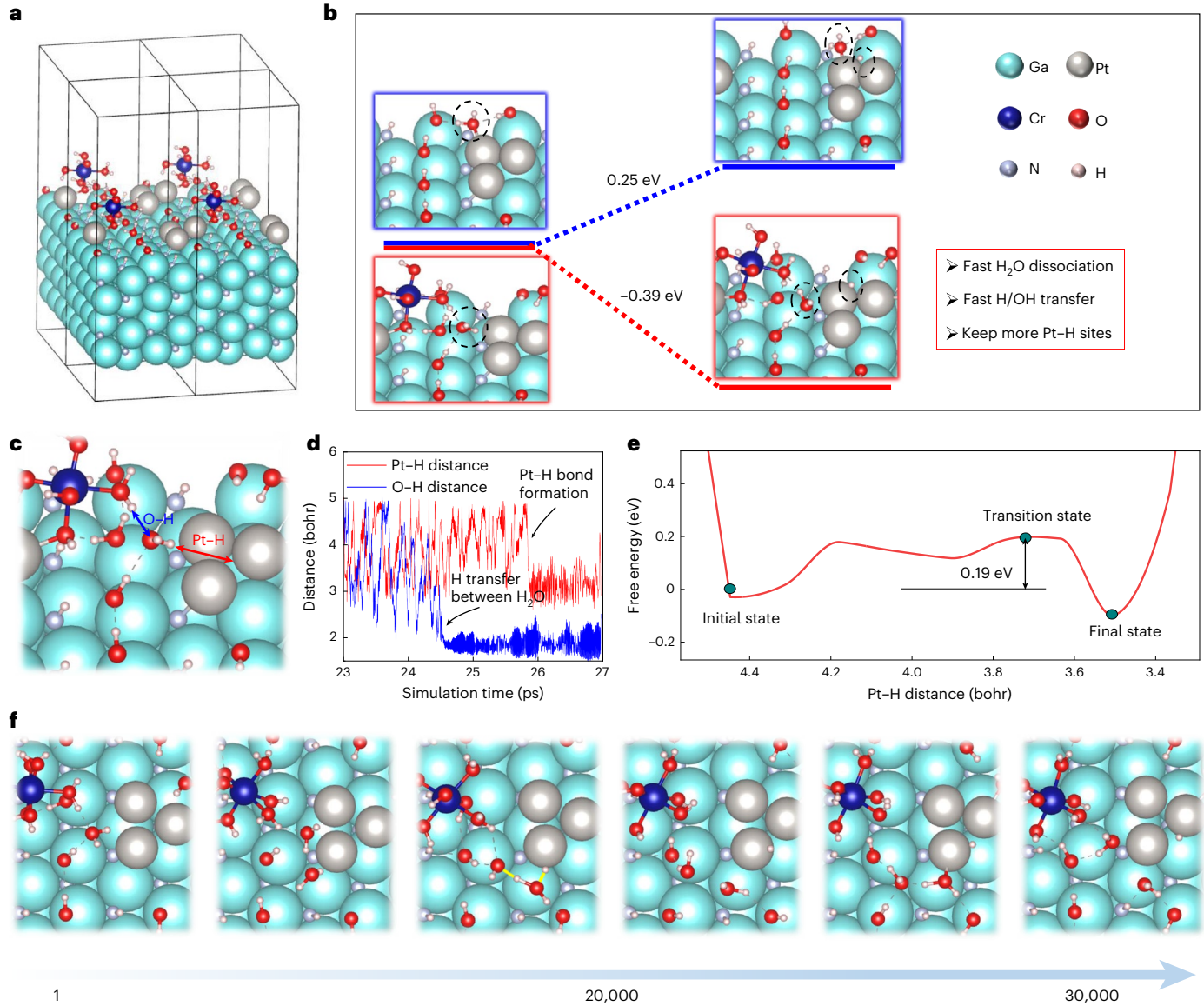


Fig. 5 | Mechanism simulation. a, The DFT model of $Cr(OH)_x$–Pt/GaN. **b**, DFT-calculated reaction energy changes for the Volmer step on $Cr(OH)_x$–Pt/GaN (red) and Pt/GaN (blue), illustrating differences in energy barriers and reaction pathways. **c**, The model for indicating the Pt–H and O–H in interfacial water for AIMD simulation. **d**, The time-evolved bond distances during the Volmer step on $Cr(OH)_x$–Pt/GaN. **e**, Free energy changes as a function of Pt–H distance along the interfacial water dissociation. **f**, The representative AIMD structures selected from >30,000 evolved models.

Conclusion

This study introduces a subnanometre interfacial hydrogen-pump-like mechanism enabled by triple-interface structure, offering a promising approach to efficient and sustainable hydrogen production through neutral seawater splitting. By efficiently coupling water activation, hydrogen transfer and Pt–H formation across adjacent interfaces for a fast hydrogen pumping process, the system dramatically enhances HER kinetics. The designed $Cr(OH)_x$–Pt/GaN photocathode achieves high photocurrent density (-100 mA cm^{-2}) and stability (>50 h) under concentrated sunlight at 0 V versus RHE, enabling a bias-free photocurrent density (-70 mA cm^{-2}) in a hydrazine-assisted seawater photoelectrolyser. This work represents a promising step forward in overcoming the challenges of neutral water splitting, providing a scalable and practical pathway for renewable hydrogen production technologies from more widely distributed water sources.

Methods

Fabrication of GaN NW/Si

Commercial 2-inch Si wafers (WRS Materials, resistivity 1–10 Ω cm) were used as the substrates for constructing n^+–p Si junctions. The junctions were fabricated by thermal dopant diffusion. In brief, boron- and phosphorus-containing spin-on dopant sources (2 ml each; BDC1-2000 and PDC1-2000, Futurrex) were sequentially deposited onto the Si substrates to define the p- and n-type regions, respectively. Dopant activation and diffusion were subsequently carried out in an Ar-filled tube furnace at 950 °C for 4 h, with a heating ramp of 25 °C min^{-1}. After thermal treatment, the wafers were immersed in a buffered oxide etchant to remove the surface oxide layer and residual dopant-derived species.

Before molecular beam epitaxy, the junction substrates were thoroughly cleaned with acetone and methanol and then transferred into the growth chamber. GaN NWs were directly grown on the Si junctions using a Veeco GEN II radio-frequency plasma-assisted molecular beam epitaxy system. The NW growth was performed at approximately 790 °C, with a nitrogen flow rate of 1.0 cm^3 min^{-1}. During growth, the Ga beam-equivalent pressure was maintained at 5×10^{-8} torr, while the radio-frequency plasma source was operated at a forward power of 350 W. The epitaxial growth continued for 2 h. Such growth conditions favour an N-terminated GaN surface, thereby providing

abundant surface nitrogen coordination sites, consistent with our previous studies[8,33].

Photodeposition of catalysts

The as-prepared GaN/Si substrate was mounted on a Teflon holder and placed in a sealed glass reactor equipped with a quartz irradiation window. The reactor was then filled with a precursor solution containing 10 µl of 0.2 M chloroplatinic acid hydrate (99.9%, Sigma-Aldrich), 10 µl of 0.2 M chromium nitrate hydrate (99.9%, Sigma-Aldrich), 50 ml of deionized water and 10 ml of methanol. Methanol was used as a sacrificial hole scavenger to facilitate the photodeposition process. Before irradiation, the reactor was evacuated for 2 min using a vacuum pump to remove residual air and minimize interference from dissolved oxygen. The GaN/Si substrate was subsequently illuminated with a 300-W Xe lamp for 30 min to induce the in situ photodeposition of Pt and $Cr(OH)_x$ species onto the GaN surface. After photodeposition, the resulting $Cr(OH)_x$–Pt/GaN/Si photocathode was removed from the reactor, thoroughly rinsed with deionized water to eliminate residual precursor species, and dried under ambient conditions before further characterization and PEC measurements. The other photocathodes with different Pt sizes were prepared by varying the amount of chloroplatinic acid hydrate solution added from 2 to 15 µl (2, 5 and 15 µl).

PEC measurements

To facilitate electrical contact, a Ga–In eutectic alloy (Sigma-Aldrich) was uniformly coated on the backside of the GaN NWs/Si substrate, followed by attachment of a copper wire as the current collector. The exposed edges and electrical contact region were sealed with chemically resistant epoxy (Loctite EA-615) and then dried overnight at room temperature, leaving the frontside of the GaN NWs/Si with an area of 0.05–0.15 cm^2. PEC measurements were conducted using either a conventional single-compartment cell or a flow-cell configuration with the compartments separated by a Nafion 117 membrane. The membrane was sequentially treated in 5% H_2O_2 at 80 °C for 1 h, deionized water at 80 °C for 1 h, and 0.05 M H_2SO_4 for 1 h, and then stored in deionized water. All electrochemical measurements were carried out using an IviumStat electrochemical workstation in a three- or two-electrode configuration, with the prepared GaN NWs/Si-based electrode as the working electrode, an Ag/AgCl electrode (3.5 M KCl) as the reference electrode. Pt gauze and RuO_x/Ti worked as the counter electrode in the three- and two-electrode system, respectively.

The electrolyte was either 0.5 M NaCl (Sigma-Aldrich) aqueous solution or simulated seawater prepared using commercial sea salts (manufactured by Instant Ocean). The major ionic composition of the commercial sea salt was comparable to that of natural seawater, containing approximately 31.3 wt% Na, 55.8 wt% Cl, 3.8 wt% Mg, 1.1 wt% Ca and 7.8 wt% SO_4^{2-}. In total, 35 g of commercial sea salt was dissolved in 1 l of deionized water. A seawater electrolyte containing 0.1 M N_2H_4 (Sigma-Aldrich) was prepared for the bias-free test. The volume of electrolytes is 200 ml for a single-cell test and each of 500 ml for catholyte and anolyte in the two-cell flow test. For flow-cell measurements, the electrolyte was circulated at 10 ml min^{-1} using a Masterflex Ismatec microflow pump (Cole-Parmer). The catholyte and anolyte were continuously recirculated through a closed-loop system connected to a sealed reservoir to maintain stable electrolyte circulation during prolonged operation.

Illumination was provided by an LCS-100 solar simulator (Oriel) equipped with an AM 1.5 G filter, with the incident light intensity adjusted according to the specific experimental conditions. Unless otherwise specified, the photocathode was illuminated from the front side throughout the PEC measurements. Photocurrent–potential curves were recorded by LSV at a scan rate of 50 mV s^{-1}. The measured potentials versus Ag/AgCl ($V_{Ag/AgCl}$) were converted to the RHE scale according to the Nernst equation: $V_{RHE} = V_{Ag/AgCl} + 0.197 + 0.0592 \times pH$. The pH values of the electrolytes were measured using a pH meter (Mettler Toledo). All measurements were performed at room temperature under ambient pressure. The evolved gaseous products were collected in a gas-tight chamber and analysed using gas chromatography (Shimadzu GC-8A).

Morphological and structural characterization

The morphological analysis of the samples was conducted using a TESCAN MIRA fourth-generation scanning electron microscope. STEM-HAADF was performed using a TFS probe-corrected Spectra 300 S/TEM, operating at 300 keV with a beam current of approximately 80 pA. Elemental mapping images were obtained through energy-dispersive EDS using a Thermo Fisher Scientific Talos F200X S/TEM with a Super-X detector. For STEM- HAADF and EDS measurements, the GaN NWs were carefully scraped off the substrate and transferred onto holy carbon film-coated copper mesh grids.

XPS measurements were carried out using a Kratos Axis Ultra XPS system, equipped with a monochromatic Al source, operating at approximately 10 mA and 15 V. ATR-FTIR spectra were recorded using a Bruker INVENIO FTIR spectrometer to analyse the surface species.

XAS measurements were conducted at Beamline 20-BM of the Advanced Photon Source. The XANES and EXAFS data were analysed using the Athena and Artemis modules within the IFEFFIT software package. A k^3-weighting and a R_{bkg} value of 1.0 were applied during data processing. Quantitative structural parameters were extracted by least-squares curve fitting of the EXAFS spectra using the Artemis module.

Computational details

Spin-polarized DFT calculations were performed to determine reaction energies using the Vienna Ab Initio Simulation Package (VASP) 5.4.1[49–51]. The projector-augmented wave method[51,52] and the Perdew–Burke–Ernzerhof exchange–correlation functional[53] were used for all geometry optimizations at the Γ point. Solvent effects were incorporated using the VASPsol extension, with a dielectric constant 78.4 to simulate the aqueous environment. A plane-wave energy cutoff of 450 eV and Gaussian smearing with $\sigma = 0.1$ were used. To account for van der Waals interactions, Grimme's DFT-D3 dispersion correction with Becke–Johnson damping[54] was applied. The convergence criteria were set to 0.01 eV $Å^{-1}$ for residual forces and 10^{-6} eV for energy. Snapshots of the computational structural models are provided in Supplementary Fig. 50. The GaN slab was modelled along the [1$\bar{1}$00] surface, as detailed in previous work[55]. A vacuum gap of at least 15 Å was included to prevent spurious interactions between periodic images. All visualizations were performed using the VESTA program.

BOMD simulations

To study the Volmer step and the dynamic migration of H/OH species at the $Cr(OH)_x$–Pt–GaN triple-interface region, a simulation system containing one $Cr(OH)_x$ complex, three Pt atoms and several H_2O molecules with the [1–100] GaN surface (10.4 Å × 12.8 Å × 30 Å) was constructed. Due to computational limitations, a small Pt_3 cluster was used to represent the ~1.5-nm Pt NP. Using a larger Pt cluster would have substantially increased the model size beyond feasible computational resources. Moreover, as the focus of this simulation is on water dissociation and the migration behaviour of H and OH species, the Pt_3 cluster provides a reasonable approximation. Its proton affinity is comparable to that of larger Pt NPs[56], making it suitable for capturing the essential interfacial reaction characteristics within the scope of this study.

Periodic boundary conditions were adopted in all three dimensions in the simulated system. All the Born–Oppenheimer molecular dynamics (BOMD) simulations based on DFT were performed using the CP2K package with the QUICKSTEP module[57]. The Perdew–Burke–Ernzerhof functional along with Grimme's van der Waal correction (D3) was used[52,58]. The Goedecker–Teter–Hutter norm-conserved pseudopotentials were used with a small core double ζ basis set[59]. An energy cutoff

of 280 Ry was used for the plane-wave basis set. The NVT ensemble was applied for the BOMD simulations coupled with Nosé–Hoover chain method that can maintain the temperature of the simulation system at approximately 300 K. The time step was set to 1.0 fs. The metadynamics method was used to determine the reaction mechanisms and free energy profiles[60]. Similar BOMD methods coupled with metadynamics samplings have already been adopted for investigating chemical reactions in some previous studies[61–63]. All visualizations were performed using the VMD and VESTA programs.

Data availability

All data supporting the findings of this study are available within the article and its Supplementary Information. Source data are available at the University of Michigan (https://doi.org/10.7302/nc1p-7h43).

References

1. van Ruijven, B. J., De Cian, E. & Sue Wing, I. Amplification of future energy demand growth due to climate change. *Nat. Commun.* **10**, 2762 (2019).
2. Martins, F. P., De-León Almaraz, S., Botelho Junior, A. B., Azzaro-Pantel, C. & Parikh, P. Hydrogen and the sustainable development goals: synergies and trade-offs. *Renew. Sustain. Energy Rev.* **204**, 114796 (2024).
3. Hansora, D. et al. All-perovskite-based unassisted photoelectrochemical water splitting system for efficient, stable and scalable solar hydrogen production. *Nat. Energy* **9**, 272–284 (2024).
4. Landman, A. et al. Photoelectrochemical water splitting in separate oxygen and hydrogen cells. *Nat. Mater.* **16**, 646–651 (2017).
5. Sokol, K. P. et al. Bias-free photoelectrochemical water splitting with photosystem II on a dye-sensitized photoanode wired to hydrogenase. *Nat. Energy* **3**, 944–951 (2018).
6. Wang, Y. et al. A single-junction cathodic approach for stable unassisted solar water splitting. *Joule* **3**, 2444–2456 (2019).
7. Zeng, G. et al. Development of a photoelectrochemically self-improving Si/GaN photocathode for efficient and durable H_2 production. *Nat. Mater.* **20**, 1130–1135 (2021).
8. Xiao, Y. et al. Oxynitrides enabled photoelectrochemical water splitting with over 3,000 hrs stable operation in practical two-electrode configuration. *Nat. Commun.* **14**, 2047 (2023).
9. Balog, Á et al. Paired photoelectrochemical conversion of CO_2/H_2O and glycerol at high rate. *Nat. Catal.* **7**, 522–535 (2024).
10. Yu, W. et al. Investigations of the stability of etched or platinized p-InP(100) photocathodes for solar-driven hydrogen evolution in acidic or alkaline aqueous electrolytes. *Energy Environ. Sci.* **14**, 6007–6020 (2021).
11. Kim, J. et al. A red-light-powered silicon nanowire biophotochemical diode for simultaneous CO_2 reduction and glycerol valorization. *Nat. Catal.* **7**, 977–986 (2024).
12. Tan, J. et al. Hydrogel protection strategy to stabilize water-splitting photoelectrodes. *Nat. Energy* **7**, 537–547 (2022).
13. Xiao, Y. et al. Band structure engineering and defect control of Ta_3N_5 for efficient photoelectrochemical water oxidation. *Nat. Catal.* **3**, 932–940 (2020).
14. Tayyebi, A. et al. Bias-free solar NH_3 production by perovskite-based photocathode coupled to valorization of glycerol. *Nat. Catal.* **7**, 510–521 (2024).
15. Kawde, A. et al. Photo-electrochemical hydrogen production from neutral phosphate buffer and seawater using micro-structured p-Si photo-electrodes functionalized by solution-based methods. *Sustain. Energy Fuels* **2**, 2215–2223 (2018).
16. Wan, C. et al. Amorphous nickel hydroxide shell tailors local chemical environment on platinum surface for alkaline hydrogen evolution reaction. *Nat. Mater.* **22**, 1022–1029 (2023).
17. Stiber, S. et al. A high-performance, durable and low-cost proton exchange membrane electrolyser with stainless steel components. *Energy Environ. Sci.* **15**, 109–122 (2022).
18. Tong, W. et al. Electrolysis of low-grade and saline surface water. *Nat. Energy* **5**, 367–377 (2020).
19. Vos, J. G. & Koper, M. T. M. Measurement of competition between oxygen evolution and chlorine evolution using rotating ring-disk electrode voltammetry. *J. Electroanal. Chem.* **819**, 260–268 (2018).
20. Waiba, S. et al. Seawater to sustainable fuel: sunlight-driven green hydrogen generation with an atomically dispersed photocatalyst. *J. Am. Chem. Soc.* **147**, 40282–40295 (2025).
21. Ren, P., Liu, Y., Nisar, I. & Das, S. Turning sunlight and seawater into energy: photocatalytic hydrogen peroxide as a green fuel carrier. *Adv. Mater.* **38**, e72660 (2026).
22. Yu, L., Ning, M., Wang, Y., Yuan, C. & Ren, Z. Direct seawater electrolysis for hydrogen production. *Nat. Rev. Mater.* **10**, 857–873 (2025).
23. Zhang, D., Shi, Y., Yin, J. & Lai, J. Recent advances for seawater hydrogen evolution. *ChemCatChem* **16**, e202301305 (2024).
24. Strmcnik, D. et al. Improving the hydrogen oxidation reaction rate by promotion of hydroxyl adsorption. *Nat. Chem.* **5**, 300–306 (2013).
25. Chen, M. et al. Hydroxide diffuses slower than hydronium in water because its solvated structure inhibits correlated proton transfer. *Nat. Chem.* **10**, 413–419 (2018).
26. Zhou, Z. et al. Electrocatalytic hydrogen evolution under neutral pH conditions: current understandings, recent advances, and future prospects. *Energy Environ. Sci.* **13**, 3185–3206 (2020).
27. Guo, J. et al. Direct seawater electrolysis by adjusting the local reaction environment of a catalyst. *Nat. Energy* **8**, 264–272 (2023).
28. Chen, J. et al. Reversible hydrogen spillover in Ru-WO_{3-x} enhances hydrogen evolution activity in neutral pH water splitting. *Nat. Commun.* **13**, 5382 (2022).
29. Zheng, X. et al. Tailoring a local acid-like microenvironment for efficient neutral hydrogen evolution. *Nat. Commun.* **14**, 4209 (2023).
30. Yu, L. et al. Hydrogen generation from seawater electrolysis over a sandwich-like NiCoN|Ni_xP|NiCoN microsheet array catalyst. *ACS Energy Lett.* **5**, 2681–2689 (2020).
31. Gao, X. et al. Karst landform-featured monolithic electrode for water electrolysis in neutral media. *Energy Environ. Sci.* **13**, 174–182 (2020).
32. Zhao, Y. et al. Charge state manipulation of cobalt selenide catalyst for overall water electrolysis. *Adv. Energy Mater.* **8**, 1801926 (2018).
33. Zhang, B. et al. Interfacially coupled Cu-cluster/GaN photocathode for efficient CO_2 to ethylene conversion. *Nat. Synth.* **3**, 1567–1576 (2024).
34. Kang, B. et al. Stable water splitting using photoelectrodes with a cryogelated overlayer. *Nat. Commun.* **15**, 1495 (2024).
35. Arunachalam, M., Kanase, R. S., Zhu, K. & Kang, S. H. Reliable bi-functional nickel-phosphate/TiO_2 integration enables stable n-GaAs photoanode for water oxidation under alkaline condition. *Nat. Commun.* **14**, 5429 (2023).
36. Gu, J. et al. A graded catalytic–protective layer for an efficient and stable water-splitting photocathode. *Nat. Energy* **2**, 16192 (2017).
37. Yang, J., Baker, A. G., Liu, H., Martens, W. N. & Frost, R. L. Size-controllable synthesis of chromium oxyhydroxide nanomaterials using a soft chemical hydrothermal route. *J. Mater. Sci.* **45**, 6574–6585 (2010).
38. Tang, C. et al. Energy-saving electrolytic hydrogen generation: Ni_2P nanoarray as a high-performance non-noble-metal electrocatalyst. *Angew. Chem. Int. Ed.* **56**, 842–846 (2017).

39. Zhang, J.-Y. et al. Anodic hydrazine oxidation assists energy-efficient hydrogen evolution over a bifunctional cobalt perselenide nanosheet electrode. *Angew. Chem. Int. Ed.* **57**, 7649–7653 (2018).
40. Zhang, T. et al. Tailoring *H intermediate coverage on the $CuAl_2O_4$/CuO catalyst for enhanced electrocatalytic CO_2 reduction to ethanol. *Angew. Chem. Int. Ed.* **62**, e202302096 (2023).
41. Chen, W. et al. Deciphering the alternating synergy between interlayer Pt single-atom and NiFe layered double hydroxide for overall water splitting. *Energy Environ. Sci.* **14**, 6428–6440 (2021).
42. Li, J. et al. A fundamental viewpoint on the hydrogen spillover phenomenon of electrocatalytic hydrogen evolution. *Nat. Commun.* **12**, 3502 (2021).
43. Osawa, M., Tsushima, M., Mogami, H., Samjeské, G. & Yamakata, A. Structure of water at the electrified platinum–water interface: a study by surface-enhanced infrared absorption spectroscopy. *J. Phys. Chem. C* **112**, 4248–4256 (2008).
44. Sun, Q. et al. Understanding hydrogen electrocatalysis by probing the hydrogen-bond network of water at the electrified Pt–solution interface. *Nat. Energy* **8**, 859–869 (2023).
45. Yao, Y., Zhu, S., Wang, H., Li, H. & Shao, M. A spectroscopic study on the nitrogen electrochemical reduction reaction on gold and platinum surfaces. *J. Am. Chem. Soc.* **140**, 1496–1501 (2018).
46. Ni, W. et al. Synergistic interactions between PtRu catalyst and nitrogen-doped carbon support boost hydrogen oxidation. *Nat. Catal.* **6**, 773–783 (2023).
47. Zhang, B. et al. A strongly coupled Ru–CrO_x cluster–cluster heterostructure for efficient alkaline hydrogen electrocatalysis. *Nat. Catal.* **7**, 441–451 (2024).
48. Li, P. et al. Hydrogen bond network connectivity in the electric double layer dominates the kinetic pH effect in hydrogen electrocatalysis on Pt. *Nat Catal* **5**, 900–911 (2022).
49. Kresse, G. & Furthmüller, J. Efficiency of ab-initio total energy calculations for metals and semiconductors using a plane-wave basis set. *Comp. Mater. Sci.* **6**, 15–50 (1996).
50. Kresse, G. & Furthmüller, J. Efficient iterative schemes for ab initio total-energy calculations using a plane-wave basis set. *Phys. Rev. B* **54**, 11169–11186 (1996).
51. Kresse, G. & Joubert, D. From ultrasoft pseudopotentials to the projector augmented-wave method. *Phys. Rev. B* **59**, 1758–1775 (1999).
52. Blöchl, P. E. Projector augmented-wave method. *Phys. Rev. B* **50**, 17953–17979 (1994).
53. Perdew, J. P., Burke, K. & Ernzerhof, M. Generalized gradient approximation made simple. *Phys. Rev. Lett.* **77**, 3865–3868 (1996).
54. Grimme, S., Ehrlich, S. & Goerigk, L. Effect of the damping function in dispersion corrected density functional theory. *J. Comput. Chem.* **32**, 1456–1465 (2011).
55. Chan, C. Y. et al. Demystifying metal-assisted chemical etching of GaN and related heterojunctions. *Appl. Phys. Rev.* **11**, 021416 (2024).
56. Tan, H. et al. Engineering a local acid-like environment in alkaline medium for efficient hydrogen evolution reaction. *Nat. Commun.* **13**, 2024 (2022).
57. Kuhne, T. D. et al. CP2K: an electronic structure and molecular dynamics software package—Quickstep: efficient and accurate electronic structure calculations. *J. Chem. Phys.* **152**, 194103 (2020).
58. Grimme, S., Antony, J., Ehrlich, S. & Krieg, H. A consistent and accurate ab initio parametrization of density functional dispersion correction (DFT-D) for the 94 elements H-Pu. *J. Chem. Phys.* **132**, 154104 (2010).
59. Krack, M. Pseudopotentials for H to Kr optimized for gradient-corrected exchange-correlation functionals. *Theor. Chem. Acc.* **114**, 145–152 (2005).
60. Laio, A. & Parrinello, M. Escaping free energy minima. *Proc. Natl Acad. Sci. USA* **99**, 12562–12566 (2002).
61. Jiang, Q. et al. Rapid N_2O formation from N_2 on water droplet surfaces. *Angew. Chem. Int. Ed.* **64**, e202421002 (2025).
62. Xia, D. et al. Spontaneous degradation of the 'forever chemicals' perfluoroalkyl and polyfluoroalkyl substances (PFASs) on water droplet surfaces. *J. Am. Chem. Soc.* **146**, 11266–11271 (2024).
63. Zhang, W. et al. Mechanism for rapid conversion of amines to ammonium salts at the air–particle interface. *J. Am. Chem. Soc.* **143**, 1171–1178 (2021).

Acknowledgements

We acknowledge the technical support from the Lurie Nanofabrication Facility and the Michigan Center for Materials Characterization. The TFS Spectra 300 and TFS Talos F200 S/TEMs were operated on the Michigan Center for Materials Characterization supported by the College of Engineering at the University of Michigan.

Author contributions

B.Z. and Z.M. conceived of this project. V.S.B. and Z.M. supervised the project. B.Z. designed the catalyst system and carried out experiments. K.L. helped with PEC data collection and analysis. V.S.B. directed and Z.L. and J.P.M. performed DFT calculations. G.-L.X., S.Z. and C.S. helped with XAS measurements. J.S.F. directed and D.X. performed AIMD simulations. B.Z. and Z.M. participated in discussion of the theoretical calculations. Y.P. prepared n^+–p Si solar cell and performed MBE growth of n^+-GaN NWs on Si. Z.Y. and K.L. helped in material characterizations. K.S. helped with STEM measurements. All the authors contributed to the overall scientific discussions and edited the paper. The paper was written by B.Z. and Z.M. with contributions from all authors.

Funding

The authors disclose support for the research of this work from the United States Army Research Office Award (grant no. W911NF2110337) and National Science Foundation (grant no. 2330525). This research used resources of the Advanced Photon Source, a US Department of Energy (DOE) Office of Science User Facilities operated for the DOE Office of Science by Argonne National Laboratory under contract no. DE-AC02-06CH11357.

Competing interests

Some IP related to this work has been licensed to NX Fuels, Inc., which was co-founded by Z.M. The University of Michigan and Z.M. have a financial interest in the company. The other authors declare no competing interests.

Additional information

Supplementary information The online version contains supplementary material available at https://doi.org/10.1038/s44160-026-01179-1.

Correspondence and requests for materials should be addressed to Bingxing Zhang, Deming Xia, Victor S. Batista or Zetian Mi.

Peer review information *Nature Synthesis* thanks Yong Wang and the other, anonymous, reviewer(s) for their contribution to the peer review of this work. Primary Handling Editor: Bei Zhang, in collaboration with the *Nature Synthesis* team.

Reprints and permissions information is available at www.nature.com/reprints.

Publisher's note Springer Nature remains neutral with regard to jurisdictional claims in published maps and institutional affiliations.

Springer Nature or its licensor (e.g. a society or other partner) holds exclusive rights to this article under a publishing agreement with the author(s) or other rightsholder(s); author self-archiving of the accepted manuscript version of this article is solely governed by the terms of such publishing agreement and applicable law.

© The Author(s), under exclusive licence to Springer Nature Limited 2026